Solar RRL
www.solar-rrl.com

Simultaneous Improvement of the Long-Term and Thermal Stability of the Perovskite Solar Cells Using 2,3,4,5, 6-Pentafluorobenzoyl Chloride (PFBC)-Capped ZnO Nanoparticles Buffer Layer

Irfan Ismail, Junfeng Wei, Xue Sun, Wusong Zha, Maria Khalil, Lianping Zhang, Rong Huang, Zhenjie Chen, Yanbin Shen, Fangsen Li, Qun Luo, and Chang-Qi Ma**

Stability is a big issue for the commercialization of perovskite solar cells. The degradation of perovskite solar cells is a complex physical–chemical process related to the photoactive layer, the interface layer, and the metal electrode. Zinc oxide (ZnO) is a popular material used as the electron-transporting layer (ETL) in perovskite solar cells. A major problem of the ZnO ETL for perovskite solar cells is the thermal instability caused by the chemical reaction between ZnO and perovskite layer. Aiming to solve the degradation issue of perovskite solar cells a kind of ZnO nanoparticle that is chemically tailored with 2,3,4,5, 6-pentafluorobenzoyl chloride (ZnO@PFBC) is provided. Herein, the migration of halogen and zinc that takes responsibility for the thermal degradation of the p–i–n-type perovskite solar cells through time of flight secondary-ion mass spectrometry (ToF–SIMS) and X-ray photoelectron spectroscopy (XPS) results is proved. Using ZnO@PFBC as a modifier of $PC_{61}BM$, both the ion migration and the chemical reaction of ZnO and perovskite are suppressed. The thermal stability and long-term illumination stability both in N_2 and in ambient conditions are simultaneously improved, 75% of the initial efficiency remaining after 200 h of annealing at 85 °C.

1. Introduction

Research progress of hybrid organic–inorganic perovskite (PVSK) solar cells has achieved fast growth in a short period of time by academia. Due to interface engineering and optimizing fabrication techniques, power conversion efficiency (PCE) of single-junction PVSK solar cells ascended substantially from 3.8% to 25.2% in a very short period, showing a great potential candidate for future photovoltaics.[1,2] So, at this circumstance, stability is a key problem that decides future commercialization.[3–5]

The degradation of PVSK solar cells is a complex physical–chemical process. The previous works reported that ion migration was a main factor that causes the intrinsic degradation of perovskite solar cells.[6–8] In perovskite solar cells, I^- and methylammonium iodide (MAI) can be transferred from the perovskite layer into the interface layer and electrode through grain boundary[9] and weak points of the buffer layers.[10] Therefore, besides the compositions[11] and crystallization of the perovskite layer,[12,13] the interface contact[14–17] and the electrodes[18,19] also greatly influenced the lifetime of the devices. In the inverted p–i–n-type perovskite solar cells, the electron-transporting layer (ETL) plays a critical role in collecting the charge, and it is also actually the structural encapsulation layer to protect perovskite layer from environmental stresses that can degrade the perovskite layer. The commonly used ETL in the p–i–n-type perovskite solar cells is fullerene derivative, typically like $PC_{61}BM$. However, the randomly oriented fullerene ETL was not robust enough to resist ion migration and ensure high stability.[20,21] The intensive reaction of PVSK and metal electrode still occurred as the $PC_{61}BM$ was deposited underneath the electrodes, especially in atmosphere air.[22,23] In the past few years, several attempts have been made to enhance the protection of the perovskite layer by applying different organic–inorganic groups as a replacement or modifier of $PC_{61}BM$.[24–26] These extended buffer layers provide a push to stabilize solar cells in ambient conditions. Due to the advantages of electron mobility and fabrication ease, metal oxides are considered choices for the

I. Ismail
University of Chinese Academy of Sciences
19 A Yuquan Rd., Shijingshan District, Beijing 100049, P. R. China

I. Ismail, Dr. J. Wei, Dr. X. Sun, W. Zha, L. Zhang, Dr. R. Huang, Z. Chen, Dr. Y. Shen, Dr. F. Li, Dr. Q. Luo, Prof. C.-Q. Ma
Suzhou Institute of Nano-Tech and Nano-Bionics
Chinese Academy of Sciences
Suzhou 215123, P. R. China
E-mail: qluo2011@sinano.ac.cn; cqma2011@sinano.ac.cn

M. Khalil
Shanghai Institute of Organic Chemistry (SIOC)
Chinese Academy of Sciences
Shanghai 200032, P. R. China

Dr. Q. Luo, Prof. C.-Q. Ma
Suzhou Institute of Nano-Tech and Nano-Bionics Nanchang
Chinese Academy of Sciences
298 Luozhu Road, Nanchang 330200, P. R. China

The ORCID identification number(s) for the author(s) of this article can be found under https://doi.org/10.1002/solr.202000289.

DOI: 10.1002/solr.202000289

interfacial encapsulation layer without affecting the performance of the photovoltaic device.[27,28] Several research groups have applied metal oxides like SnO_2,[29] ZnO,[30,31] CeO_x[32] and CrO_x[33] underlying the top electrode to create a barrier or replace the PCBM layer for moisture and oxygen to suppress the penetration-leaded degradation of the perovskite layer. Among all of them, ZnO nanoparticles (NPs) were very popularly used in the perovskite solar cells in different device architectures.[27,34–36] You et al.[31] first used ZnO as the ETL on top of the perovskite layer to replace PCBM and achieved a best efficiency of 16.1%. Bai et al.[30] and Qiu et al.[37] reported the use of ZnO NPs on top of the PCBM ETL to achieve a higher PCE. Zhao et al. used Al-doped ZnO NPs as the solution-processed top buffer layer to enhance the thermal stability.[38]

Although there are various applications of ZnO in PVSK solar cells, a major problem associated with ZnO is the fast degradation of organic–inorganic perovskite layer, especially the MAI-based films, which limited the application of ZnO in high-performance stable perovskite solar cells. Yang et al. found that the ZnO-assisted degradation of perovskite films was due to the acid–base chemical reaction of perovskite and ZnO, which would cause the decomposition of perovskite layer into PbI_2.[39] Once the films are heated, the degradation speed would be accelerated further. Only several minutes after annealing of the films would result in colour change from brown to yellow, revealing the decomposition of perovskite films.[39] Several solutions have been developed previously, including ion doping,[40] adding an interlayer,[41,42] removing the residuals ligands of the ZnO surface,[43] developing a ZnO/r-GO core–shell structure quantum dot,[44] or using the dynamic spin-coating strategy.[45] Chen and coworkers[42] used a 3-aminopropanoc acid self-assembled monolayer as a modifier of the sol–gel ZnO film, leading to the improvement of efficiency from 11.96% to 15.76%. Zheng and coworkers[46] added a thin layer of MgO and a sub-monolayer of protonated ethanolamine molecules on top of ZnO. Chang and coworkers developed low-temperature TiO_x to passivate the ZnO surface.[47] Enhanced electron transporting and stability of ZnO/PVSK interface were achieved. Yao et al.[48] took the initiative to anchor the surface of ZnO NPs with fullerene molecules, and Yang and coworkers developed the core–shell structure ZnO@SnO_2 layer.[49] These works inspiringly revealed that the ZnO-assisted degradation of the perovskite solar cells can be solved through interface engineering. We know the metal oxide NP ETLs could be easily modified using a variety of organic thin or assembled molecular layers, which can lessen the surface defects and improve the interface charge collection. However, most of the work handled this problem through film technology, whereas rare work was focused on solving the stability issue in the ZnO-based perovskite solar cells through surface chemical modifying of NPs.

In this work, dual modification concept is introduced to reduce the chemical reactivity of the surface of ZnO. ZnO NPs are initially capped with the silane coupling agent, 3-aminopropyltrimethoxy silane (APTMS), and then, the terminal group of the coupling agent is replaced with benzoyl chloride derivatives using 2,3,4,5,6-pentafluorobenzoyl chloride (PFBC) to make it available for a charge transfer bridge along with the unreactive behavior of NPs toward the perovskite layer. Using ZnO@PFBC as a modifier of the PCBM ETLs, significant improvement in the thermal stability and long-term stability of the perovskite solar cells was observed in ambient and controlled environments with the achievement of 16.93% efficiency, which is 9% higher than that of the device without any NPs and 8% higher than the devices based on the pristine ZnO NPs. In comparison with the device with sole PCBM and PCBM/ZnO ETL, the use of ZnO@PFBC layer suppressed the migration of Al from the top electrode and prevented the transporting of Zn into the perovskite layer and passivated the chemical reaction between ZnO and PVSK layer during thermal annealing. Thereby, the PCBM/ZnO@PFBC ETL-based p–i–n-type perovskite device kept 75% of the initial efficiency after annealing at 85 °C for 200 h and around 60% of the initial efficiency after 1100 h continuous illumination, which were greatly improved compared with the standard device with sole PCBM ETL. This work suggested that the dual modification strategy of metal oxide NPs potentially points to a promising new way of stabilizing PVSK solar cells with efficient charge collection.

2. Results and Discussion

The PFBC-modified ZnO (ZnO@PFBC) NPs were synthesized through two-step chemical modification. First, ZnO NPs were modified by 3-aminopropyltrimethoxy silane (APTMS, ZnO@APTMS) through surface ligand exchange of hydrogen group with triethoxysilane groups, as we have reported previously.[50] Second, ZnO@APTMS was further modified by PFBC through the chemical reaction between $-NH_2$ and chloride group. As the chemical reaction between $-NH_2$ and chloride groups is easy, it is highly efficient to obtain PFBC-capped ZnO NPs. The synthesis process of ZnO@PFBC is shown in **Scheme 1**, and the detailed experimental procedures are provided in Experimental Section.

Figure 1a,b shows the transmission electron microscopy (TEM) images of the pristine ZnO and ZnO@PFBC NPs. As shown by these images, the ZnO@PFBC NPs were better dispersed in ethanol solvent. From the dynamic light scattering (DLS) images of NPs, as shown in Figure 1c,d, we found that the average diameter of the pristine ZnO and ZnO@PFBC was all ≈4 nm. This result indicated that the modification of ZnO by PFBC does not cause a change in diameter. Note that the ZnO@PFBC NPs were dried as powder and redispersed in ethanol to form nanoink when used. Figure 1e shows the photograph of the ZnO@PFBC powers and nanoinks. It is obvious to see that the nanoinks obtained from the powder can be stable for more than 10 months without precipitates, showing quite long-time stability, whereas ZnO ink only can be stable within 1 month.[50]

The formation of ZnO@PFBC NPs was proved by Fourier transform infrared spectroscopy (FTIR) and X-ray photoelectron spectroscopy (XPS) spectra. Figure 1f shows the FTIR spectrum of the pristine ZnO and ZnO@PFBC films. In the results, both ZnO and ZnO@PFBC exhibited a sharp peak at 468 cm^{-1}, which was ascribed to the stretching vibration of Zn—O bonds. The wide peak at 3000–3500 cm^{-1} in ZnO and ZnO@PFBC films originated from surface –OH groups. Compared with the pristine ZnO NPs, the intensity of surface –OH groups was decreased. In addition, the presence of peaks at 1400 and 1685 cm^{-1} that

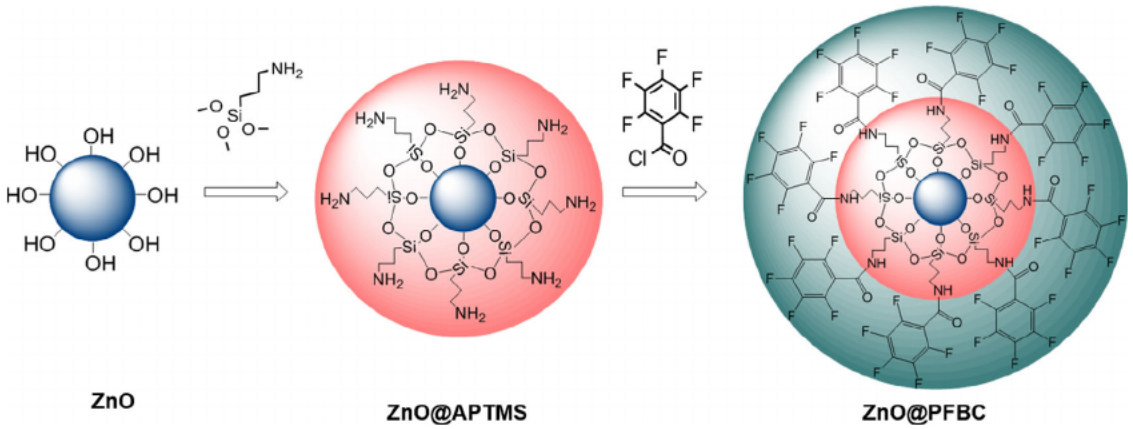

Scheme 1. Synthesis process of the ZnO@PFBC NPs.

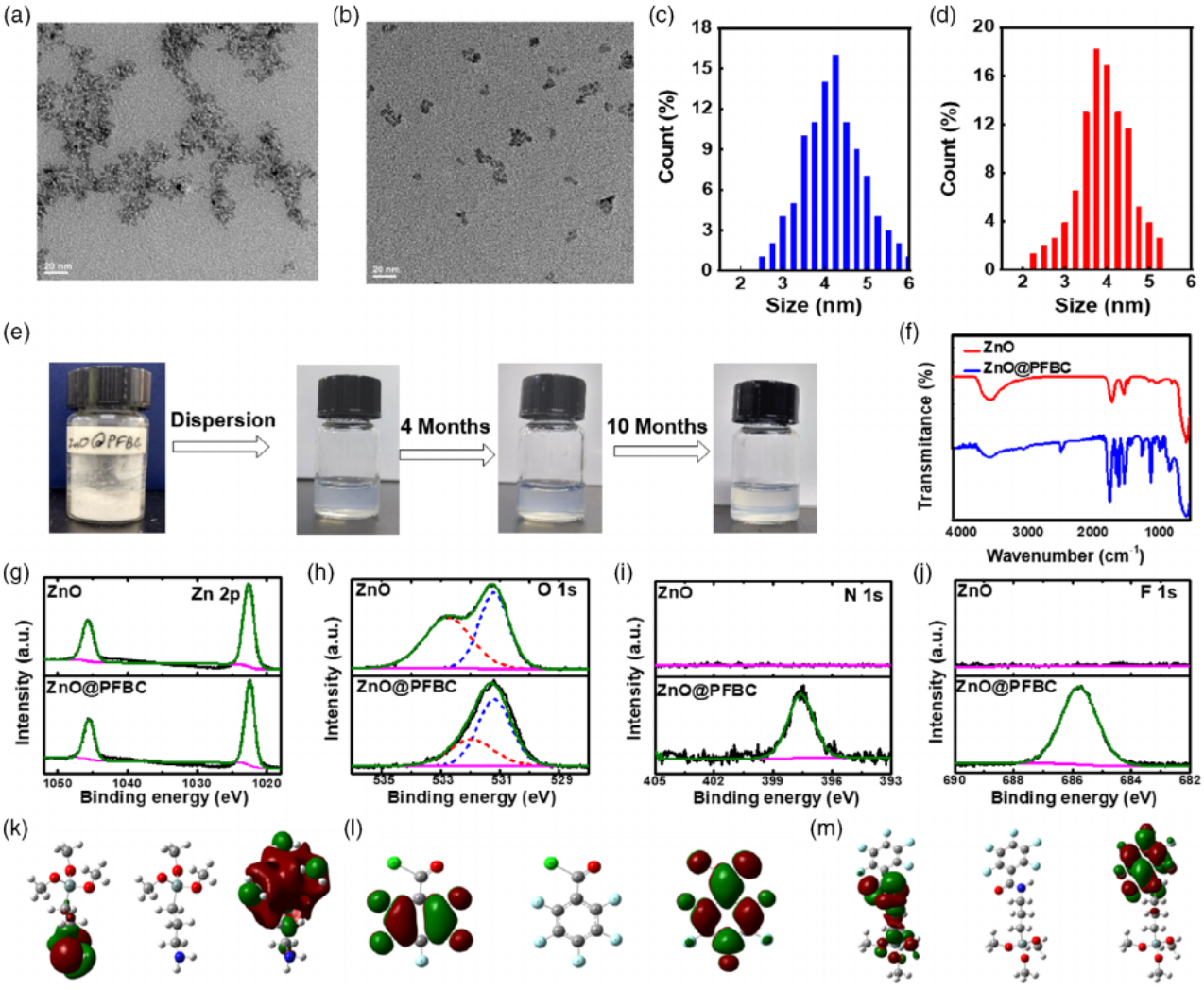

Figure 1. a,b) TEM images and c,d) DLS of the ZnO and ZnO@PFBC NPs. e) Photographs of the ZnO@PFBC NP powders and nanoinks stored in air for different months. f) FTIR spectra of the ZnO and ZnO@PFBC NPs. g) Zn 2p, h) O 1s, i) N 1s, j) F 1s XPS spectra of the ZnO and ZnO@PFBC films. Computational analyses for HOMO, LUMO, and dipole moments of k) APTMS, l) PFBC, and m) APTMS@PFBC.

belong to the —COO bond indicated the existence of residual acetate groups in these NPs.[51] In addition to these peaks, an extended peak at 1006 cm^{-1} was observed in ZnO@PFBC film, which was attributed to the vibrational modes of Si–O–Si groups from APTMS.[50] The two similar and consecutives peaks at 1500 cm^{-1} exhibited two different groups of fluorine attached with benzoyl groups, which could lead to the hydrophobic character of the ZnO@PFBC NP surface. There were asymmetric and symmetric C–H stretching at 2866 and 2929 cm^{-1} in ZnO@PFBC, due to APTMS attached on the surface.[50] Figure 1g–j shows the Zn 2p, O 1s, N 1s, and F 1s XPS spectra of the ZnO and ZnO@PFBC films. XPS analysis at the high-resolution spectrum of Zn 2p deconvoluted the spin-orbit coupling for Zn 2p, and the broader signal was split into two symmetrical peaks of Zn $2p^{3/2}$ and Zn $2p^{1/2}$, located at 1022.5 and 1045.6 eV, respectively.[52] In Figure 1h, two binding signals were extracted from the asymmetric O 1s signal. In case of pristine ZnO NPs, two symmetrical signals for the higher and lower energy levels of the O 1s signals at 531.2 and 532.8 eV were ascribed to the Zn—O—Zn lattice oxygen and defect oxygen, including vacancy oxygen and zinc hydroxide in ZnO, respectively.[52,53] The ratio of the lattice oxygen and defect oxygen is ≈6:5. For the ZnO@PFBC NPs, both peaks from lattice and defect oxygen were observed. However, the intensity of defect oxygen dramatically decreased relative to the pristine ZnO films, suggesting the removal of oxygen defects. In the high-resolution scan of N 1s peaks (Figure 1i), the broad peak that appeared at 397.5 eV in ZnO@PFBC was ascribed to the remained terminal $–NH_2$ of APTMS, indicating ZnO NPs were still partly capped by APTMS after two-step sequential chemical modification. Furthermore, the signal of F 1s (Figure 1j) observed at 685.5 eV exhibited the covalent bond of F element. In addition, the intensity of the F 1s cover level (Figure S1, Supporting Information) was much higher than that of N 1s, meaning reasonable transferring conversion from ZnO@APTMS to ZnO@PFBC. Because the chemical reaction between amino and acyl chloride was easy and high speed, it is highly possible that PFBC would cap outsides the ZnO NPs through covalently bond of amino and acyl chloride. These XPS results, together with the FTIR spectra of ZnO@PFBC, proved the successful capping of ZnO by PFBC.

Density functional theory (DFT) calculation was conducted to help us understand the electronic structure change of ZnO caused by PFBC capping. As shown in Figure 1k–m, the frontier orbitals like highest occupied molecular orbital (HOMO) and lowest unoccupied molecular orbital (LUMO) energy levels and the dipole moment of the capping molecular, as well as the possible combined structure, were investigated and analyzed. As mentioned earlier, the first-step modification was processed by APTMS. As shown in Figure 1k–m, APTMS exhibited a low dipole moment around 0.82D, which is fairly low for electron extraction. The second-step modification was processed by PFBC. It was found that 2,3,4,5,6-pentafluorobenzoyl chloride (PFBC) showed the dipole moment around 2.85D, which is slightly higher as compared with APTMS. So, in this work, properties of both modifiers were combined around the metal oxide. In theoretical studies, PFBC was attached as the terminal group of APTMS, and it passed through the same analysis as 3-aminopropyltrimethoxy silane-attached 2,3,4,5,6-pentafluorobenzoyl amide (APTMS@PFBC). It was found out that the dipole moment of the new structure reached 1.42D, which was strong enough to continue the electronic activities of solar cell without disturbance. These computational analyses encouraged advancing this work, because it predicted a prospective progressing chemical approach for metal oxides to become a preferable choice for PVSK solar cells.

Figure 2 shows the morphology and photoelectric properties of the ZnO and ZnO@PFBC films. First, the atomic force microscopy (AFM) images of the films are shown in **Figure 3**a,b. Both in the ZnO and ZnO@PFBC films, we could clearly find the NPs

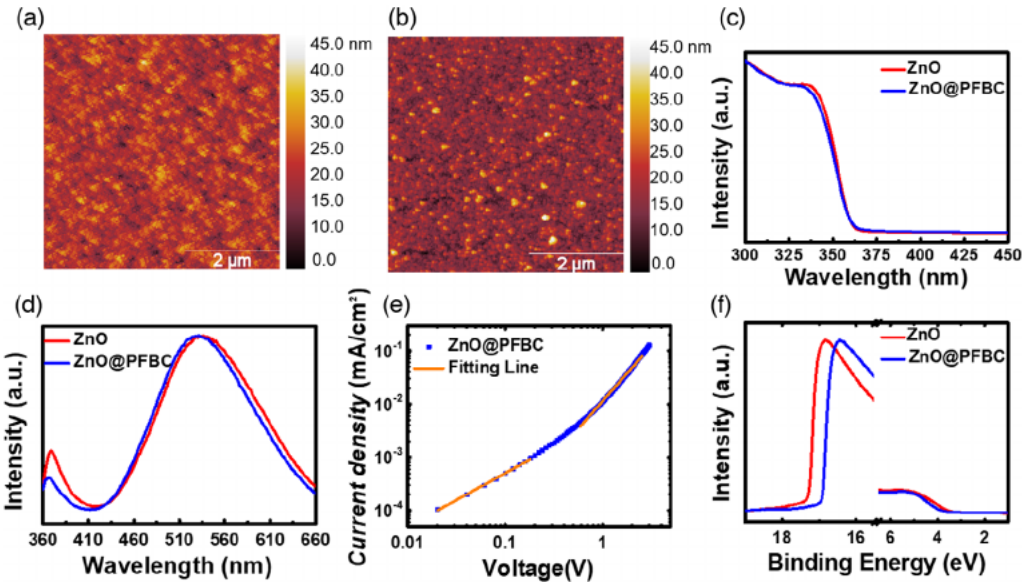

Figure 2. a,b) AFM images of the ZnO and ZnO@PFBC films. c) Absorption and d) PL spectra of the ZnO and ZnO@PFBC films. e) *J–V* characteristics of the electron-only device with the structure of ITO/Al/ZnO@PFBC/Al. f) UPS spectra of the ZnO and ZnO@PFBC films.

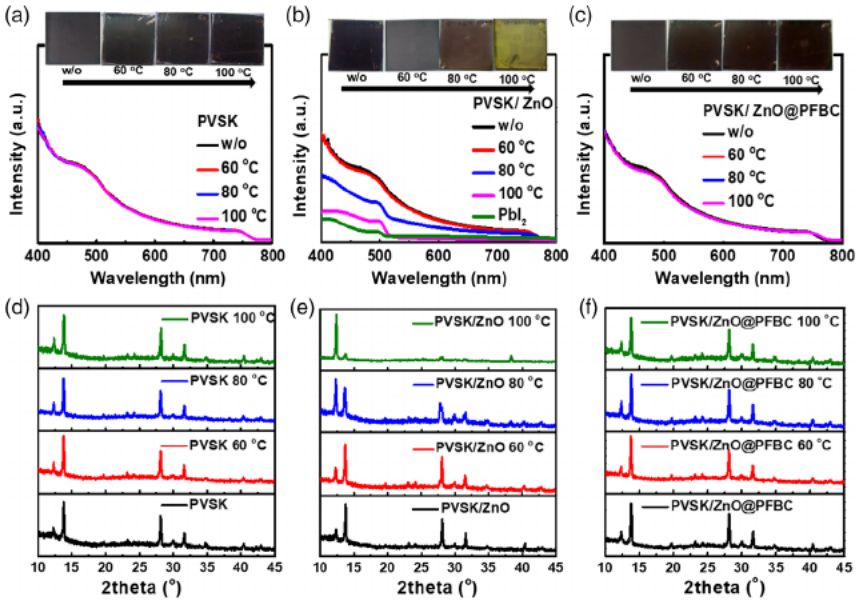

Figure 3. Absorption spectra of the a) ITO/PEDOT: PSS/PVSK, b) ITO/EPDOT: PSS/PVSK/ZnO, and c) ITO/PEDOT: PSS/PVSC/ZnO@PFBC films after annealing at different temperatures. Inset: the photographs of the films. XRD patterns of d) ITO/PEDOT: PSS/PVSK, e) ITO/PEDOT: PSS/PVSK/ZnO, and f) ITO/PEDOT: PSS/PVSK/ZnO@PFBC films after heating at different temperatures.

on top of the glass substrate, indicating good coverage and film formation properties. From the AFM images, it was found the root mean roughness (RMS) of the ZnO and ZnO@PFBC films was 4.6, and 4.5 nm, respectively. In the ZnO@PFBC film, we also observed some different NPs, which might be ascribed to the impurities due to the hydrolysis of silane during the first step of synthesis. The absorption and photoluminescence (PL) spectra of the ZnO and ZnO@PFBC films were measured and are shown in Figure 2c,d. Note that the films for absorption and PL measurements were fabricated through spin coating from the inks with the same concentration of 10 mg mL^{-1}. The absorption intensities of the ZnO@PFBC and ZnO films were nearly the same, and both the ZnO and ZnO@PFBC films presented a typical absorption with an absorbance cutoff at around 360 nm. With the excitation of 350 nm, both the pristine ZnO and ZnO@PFBC films exhibited a weak emission peak at 360 nm and a stronger emission peak centered at 530 nm. These two emission peaks could be attributed to the band edge emission and the oxygen vacancy defect-related emission.[54]

In terms of the influence of PFBC capping on the electron-transporting properties, both the electron mobility and the work function of the ZnO@PFBC films were studied. First, electron mobility was determined using the space-charge-limited current (SCLC) method through testing the *J*–*V* characteristics of the electron-only device with structure of ITO/Al/ZnO@PFBC/Al. As shown in the *J*–*V* characteristics of the device, shown in Figure 2e, we found this curve well fitted with the SCLC mode with an ohmic contact at a low bias region and the trapped space charge region at a high bias region, suggesting that the electron mobility of the ZnO@PFBC films could be calculated using this method. For the SCLC method, we know that charge mobility can be calculated from the SCLC region using the Mott–Gernery SCLC equation, described as follows.[55]

$$J = \frac{9}{8}\varepsilon_r \varepsilon_0 \mu_e \frac{V^2}{d^3}$$

where ε_r, ε_0, μ_e, and d are the relative dielectric constant of the materials, the vacuum dielectric constant, the electron mobility, and the film thickness, respectively. Herein, for ZnO@PFBC, ε_r, ε_0, μ_e, and d are the relative dielectric constant of the materials, the vacuum dialectic constant, the electron mobility, and film thickness, respectively. As a result, the electron mobility of ZnO@PFBC was estimated to be about 4.1×10^{-4} cm^2 V^{-1} S^{-1}, similar to the electron mobility of the pristine ZnO (5.88×10^{-4} cm^2 V^{-1} S^{-1}), as we have reported previously.[50] This result depicted that PFBC capping only caused a slight decrease in the charge mobility for ZnO NPs, which could enable good charge transporting in the cathode interface. Then the work function of the ZnO@PFBC film was determined from the ultraviolet photoelectron spectroscopy (UPS) result. Figure 2f shows the UPS spectra of the ZnO and ZnO@PFBC films that deposited on top of the ITO substrate. According to this figure, the work function of ZnO and ZnO@PFBC films was estimated to be about 3.92 and 4.23 eV. The increased work function of ZnO@PFBC relative to ZnO could be ascribed to the electron-withdrawing ability of F atoms. However, the work function of 4.23 eV was still suitable for matched energy alignment. According to the UPS spectra and the absorption spectra of ZnO and ZnO@PFBC, the conducting and valence bands of the ZnO and ZnO@PFBC films were estimated. Specifically, for ZnO, the conducting band and valence band energy levels are 3.85 and 7.30 eV. For ZnO@PFBC, the conducting band and valence band energy levels are 4.30 and 7.75 eV. In addition, the capping of PFBC outside ZnO NPs changed the surface energy. According to the contact angles of the films with water and diiodomethane as shown in Figure S2, Supporting Information, the surface energies of the pristine ZnO and

ZnO@PFBC were 66.16 and 36.06 mN m^{-1} (listed in Table S1, Supporting Information), respectively. The decreased surface energy of ZnO@PFBC films proved the capping PFBC again. As PFBC is highly hydrophobic, modification by such molecules is essential to improve moisture resistance.

As discussed a serious issue of ZnO for perovskite solar cells is the chemical reaction-related instability problem, especially accelerated, as it was under thermal conditions. Therefore, with the aim of solving this problem through surface chemical modification in the work, we first investigated the thermal stability of perovskite films. Figure 3a–c shows the absorption spectra of PVSK, PVSK/ZnO, and PVSK/ZnO@PFBC films after thermal treatment at different temperatures in the N_2-filled glove box. The insets of Figure 3a–c show the photographs of these films. The absorption spectra of the pure PVSK films showed negligible change after annealing at 100 °C, and the photographs showed the films were nearly unchanged. It meant that the pure PVSK film was stable enough to sustain thermal annealing within 100 °C. In contrast, the absorption intensity of the PVSK/ZnO films showed a dramatical decrease after thermal annealing at 60–100 °C. The film gradually changed from bark brown to yellow with the increase in annealing temperature. As the annealing temperature increased up to 100 °C, a totally yellow film was observed, indicating the decomposition of the perovskite films to PbI_2. However, the PVSK/ZnO@PFBC film was almost unchanged as the annealing temperature increased to 100 °C, and the film color was nearly brown. These results suggested the contact of ZnO with the perovskite films leading to the decomposition of perovskite films. However, the serious decomposition of PVSK films was suppressed through capping the ZnO with PFBC. Therefore, the chemical capping of ZnO is really a feasible strategy to suppress the chemical reaction of PVSK and ZnO.

Further, the X-ray diffraction (XRD) patterns of these films were measured to see the detailed variation of the composition and structure during annealing. As evidence of the PVSK decomposition during thermal annealing, Figure 3d–f shows the XRD patterns of the films. The peaks at 14.08°, 28.41°, and 31.85° correspond to the (110), (220), (310) planes of the PVSK crystals, and peaks at 12.65° were ascribed to PbI_2. Both in the pure PVSK and in the PVSK/ZnO@PFBC film, no diffraction peak change was observed after being thermal treated at different temperatures. Nevertheless, in the PVSK/ZnO film, we found unexpected decomposition from PVSK to PbI_2 when the thermal temperature was higher than 80 °C. Especially after thermal annealing at 100 °C, PVSK was almost totally converted to PbI_2.

Besides the conventional XRD measurements, in situ XRD measurements were also carried out to detect the circle process of PVSK during thermal annealing. The experiment process was produced as follows: PVSK, PVSK/ZnO, and PVSK/ZnO@PFBC films were put on the in situ thermal plate and annealed gradually from room temperature to 100 °C. The XRD scan was periodically conducted for each 30 min. To exclude the impact by moisture and oxygen, the samples were kept in the vacuum chamber. The detailed results of XRD patterns during in situ annealing are shown in Figure S3, Supporting Information. It could be learnt that there was no clear presence of PbI_2 peaks during heating, but there was decline in the intensity of the PVSK peaks for the PVSK films (Figure S3a, Supporting Information). In the case of ZnO on the top of the PVSK layer, there was a vast chance of the appearance of PbI_2 along with the degradation of the active layer. It is shown in Figure S3b, Supporting Information, that a little rise above the room temperature (40 °C) caused a sharp decline in the concentration of PVSK, whereas, at the same time, an obvious appearance of PbI_2 peak occurred that effectively overcomes the ratio of PVSK peak rapidly. In comparison, the passivated surface of ZnO NPs, in case of ZnO@PFBC in Figure S3c, Supporting Information, remained intact from interacting with the PVSK layer at a higher range of temperature. Modifications on the surface of metal oxides passivated the intrinsic surface defects which led to the unreactive chemical encapsulation on top of the perovskite layer.

After we have confirmed that PFBC capping of ZnO could suppress the chemical reaction between PVSK and ZnO, and significantly improve the thermal stability, we moved forward to fabricate the perovskite solar cells. Unfortunately, the perovskite solar cells with ZnO@PFBC ETL presented a low efficiency (Figure S4, Supporting Information) though the chemical reaction of ZnO and perovskite was suppressed, which might be due to the no-ideal connection between PVSK and ZnO@PFBC. The detailed reason was not fully understood yet. Previous work has reported that PCBM was important to passivate the surface defect in the PVSK grain boundaries.[56] Thus, devices with a structure of ITO/PEDOT: PSS/PVSK/PC_{61}BM/ZnO@PFBC/Al were fabricated. As ZnO@PFBC was used as a modifier of PC_{61}BM ETL, the thermal stability of the ITO/PEDOT: PSS/PVSK/PC_{61}BM/ZnO@PFBC films significantly improved as compared with the ITO/PEDOT:PSS/PVSK/PC_{61}BM/ZnO film, as shown in **Figure 4**. In this figure, we observed the gradual decomposition of the perovskite films into PbI_2 with the increase in thermal annealing temperature from 120 to 180 °C in the

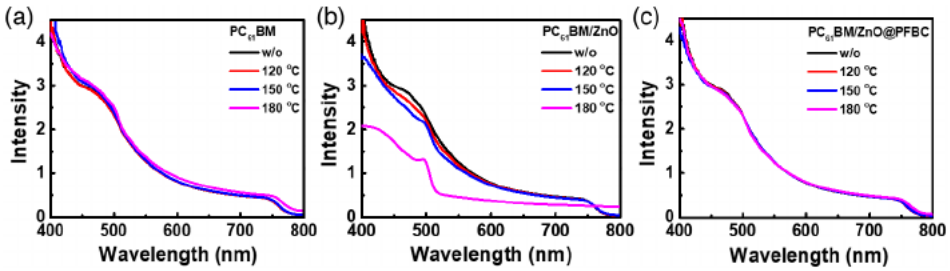

Figure 4. UV–vis absorption Spectroscopy of the films with structure of a) ITO/PEDOT: PSS/PVSK/PC_{61}BM, b) ITO/PEDOT: PSS/PVSK/PC_{61}BM/ZnO, and c) ITO/PEDOT: PSS/PVSK/PC_{61}BM/ZnO@PFBC.

ITO/PEDOT:PSS/PVSK/$PC_{61}BM$/ZnO film. Specifically, as the temperature increased to 180 °C, the absorption intensity of perovskite dramatically decreased. But, both the pristine films without ZnO and the films with ZnO@PFBC films exhibited negligible change in the absorption intensity, suggesting no decomposition of the perovskite films. These results proved the excellent thermal stability of the ITO/PEDOT:PSS/PVSK/$PC_{61}BM$/ZnO@PFBC films. Figure S5, Supporting Information, shows the dynamic XRD patterns of ITO/ PEDOT: PSS/ PVSK/ $PC_{61}BM$, ITO/ PEDOT: PSS/ PVSK/$PC_{61}BM$/ZnO, and ITO/ PEDOT: PSS/ PVSK/$PC_{61}BM$ /ZnO@PFBC films during thermal annealing from room temperature to around 140 °C. The results also showed improved stability of the ITO/ PEDOT: PSS/ PVSK/$PC_{61}BM$/ZnO@PFBC film than the ITO/ PEDOT: PSS/ PVSK/$PC_{61}BM$/ZnO film.

Figure 5a shows the device structure, where ZnO and ZnO@PFBC were deposited on the top of $PC_{61}BM$ layer as modifiers. Figure 5b shows the energy level of the device, where the conducting and valence bands were determined from UPS spectra, and the energy structure's other layers were cited from previous studies.[57] Figure 5c shows the cross-sectional scanning electron microscopy (SEM) images of the perovskite and the electrode buffer layer, where the sequential layers of ITO, PEDOT: PSS, PVSK, $PC_{61}BM$, and ZnO@PFBC were clearly observed. In addition, the thickness of the ITO, PEDOT: PSS, PVSK, $PC_{61}BM$, and ZnO@PFBC layer could be estimated at about 280, 100, 330, 35, and 15 nm from the SEM images. The *J*–*V* characteristics and external quantum efficiency (EQE) spectra of these devices are shown in Figure 5d,e, and the detailed performance parameters of these cells are shown in **Table 1**. The device with sole $PC_{61}BM$ ETLs presented an optimized PCE of 15.33% and average performance of 14.33%. For the optimized device, the open-circuit voltage (V_{OC}), short-circuit current (J_{SC}), and fill factor (FF) are 1.04 V, 19.11 mA cm^{-2},

Table 1. Device performance of the perovskite solar cells with different ETLs.

ETL	V_{OC} [V]	J_{SC} [mA cm^{-2}]	FF [%]	PCE [%]	PCE ± std. dev. [%][a)]
$PC_{61}BM$	1.04	19.11	78	15.53	14.33 ± 0.60
$PC_{61}BM$/ZnO	1.00	19.69	80	15.68	14.23 ± 0.96
$PC_{61}BM$/ZnO@PFBC	1.04	20.46	80	16.93	15.87 ± 0.75

[a)]Average value calculated over ten individual devices.

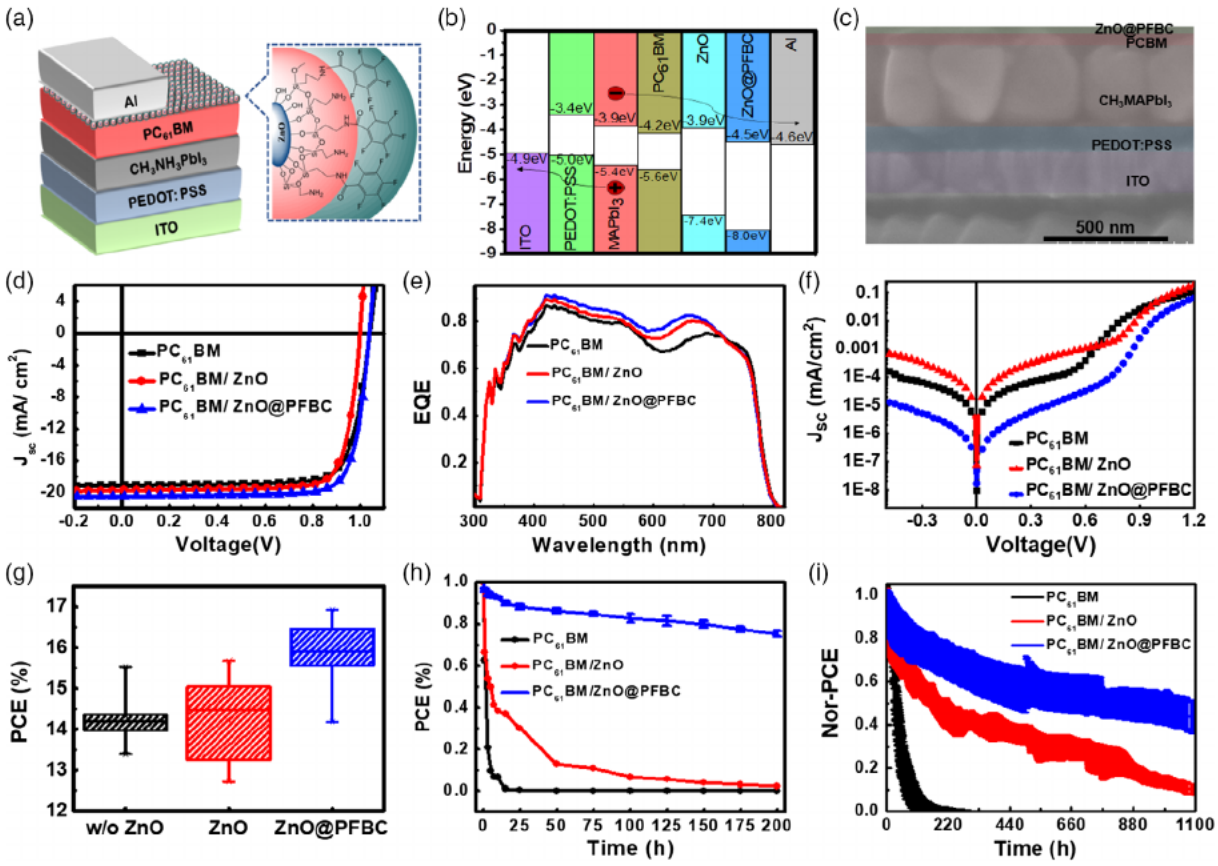

Figure 5. a) Device structure, b) energy level of the perovskite solar cells. c) cross-section SEM images of the perovskite solar cells with $PC_{61}BM$/ZnO@PFBC buffer layer. d) *J*–*V* characteristics, e) EQE spectra, f) dark *J*–*V* curves, and g) histogram of the performance with different ETLs. h) Evolution of PCE of the perovskite solar cells with different ETLs during annealing at 85 °C for 200 h in the N_2-filled glove box and i) the evolution of PCE during continuous illumination in the N_2-filled glove box at around 40 °C.

and 78%, respectively. For the cells with $PC_{61}BM$/ZnO bilayer ETL, the introduction of ZnO on the top of PCBM caused a slight increase in J_{SC} thus yielding an improved performance of 15.68%. The insertion of ZnO@PFBC between $PC_{61}BM$ and Al leads to the increase in J_{SC} to 20.46 mA cm^{-2}, and FF slightly improved to 80% as well. As a consequence, an optimized performance of 16.93% was achieved. Such a performance was nearly 18% promotion compared with the control device. Herein, the improvement of J_{SC} caused by ZnO and ZnO@PFBC layers was well proven by the EQE spectra, where increased light harvesting in the region from 600 to 700 nm was observed. Qiu et al.[37] have reported the promotion of J_{SC} by insertion of ZnO on $PC_{61}BM$ in previous studies. Figure 5f shows the dark *J–V* characteristics of these devices. From the dark *J–V* curves, one can find the improved rectification ratio of the ZnO@PFBC involved devices relative to the other two devices. The histogram of the performance for the cells with different ETLs is shown in Figure 5g. This figure shows that the reference cell using sole $PC_{61}BM$ ETL gave an average performance at ≈14%. The device with $PC_{61}BM$/ZnO ETL gave a similar average performance like the ZnO-based solar cells. But a large error bar was observed. For the $PC_{61}BM$/ZnO@PFBC ETL-based solar cell, the average performance largely increased to about 16%. From the histogram of performance, we knew that the introduction of ZnO@PFBC on $PC_{61}BM$ can generally improve the efficiency of the perovskite devices.

As introduced earlier, we know that the PVSK/ $PC_{61}BM$ and PVSK/$PC_{61}BM$ /ZnO@PFBC films have a reasonable thermal stability, whereas the PVSK/ $PC_{61}BM$ /ZnO film shows a poor property. Properly speaking, the pure PVSK film is the most stable one among the three kinds of films. However, when we moved forward to the whole device, interesting results were observed. The thermal stabilities of the perovskite solar cells with the structure of ITO/PEDOT: PSS/PVSK/$PC_{61}BM$/Al, ITO/PEDOT: PSS/PVSK/$PC_{61}BM$/ZnO/Al, and ITO/PEDOT: PSS/PVSK/$PC_{61}BM$/ZnO@PFBC/Al were investigated, and Figure 5h shows the evolution of efficiency when annealing the devices at 85 °C in the N_2-filled glove box for different time. The decay curves of V_{OC}, J_{SC}, and FF are shown in Figure S6, Supporting Information. For both the $PC_{61}BM$ and $PC_{61}BM$/ZnO ETL-based solar cells, the performance declined sharply within 20–30 h. In addition, the device with $PC_{61}BM$ ETL degraded very fast. However, the $PC_{61}BM$/ZnO@PFBC ETL-based device could resist around 200 h of continuous heating at 85 °C and kept 80% efficiency of the initial value. Herein, these results showed that the perovskite solar cells with $PC_{61}BM$/ZnO@PFBC ETL showed a much better thermal stability than the $PC_{61}BM$-based cells. As the ITO/PEDOT: PSS/PVSK/$PC_{61}BM$ films without the Al electrode showed nearly comparable thermal stability to the ITO/PEDOT: PSS/PVSK/$PC_{61}BM$/ZnO@PFBC films, the quick degradation of the ITO/PEDOT: PSS/PVSK/$PC_{61}BM$/Al device was mainly caused by the vapored Al electrode. In other words, the device stability was highly influenced by the perovskite layer, the ETL, as well as the interface contact between ETL and the top electrode.

To understand the deep reason of the Al electrode-assisted thermal degradation, the time of flight secondary-ion mass spectrometry (ToF–SIMS) of these fresh and aged devices were measured, and **Figure 6**a–c shows the results. By analyzing the changes of Al, C, Pb elements, the corresponding interfaces of Al, ZnO, $PC_{61}BM$, and $MAPbI_xCl_{3-x}$ layers were determined. In the $PC_{61}BM$ ETL-based solar cells, no change was observed for Al element, whereas, the intensity of I increased slightly in the aged cells. In addition, it seems that element I has migrated into Al and $PC_{61}BM$ layer after thermal annealing. For the device with $PC_{61}BM$/ZnO ETL, element Al seems to permeate into the PVSK and $PC_{61}BM$ layer. Meanwhile, intensive peaks of I were observed in the ZnO layer, and Zn was transported into the perovskite layer in the aged devices. These changes indicated the chemical reaction between ZnO and perovskite layer. On the side of $PC_{61}BM$/ZnO@PFBC ETL-based solar cells, both the distribution of elements Al and I showed negligible change, indicating a robust protection of Al or PVSK layer by the ZnO@PFBC layer.

Further, to confirm the reaction mechanism, surface XPS spectra of the aged films were measured. Figure 6d–f shows the core level of Al 2p XPS spectra in the aged films, and Figure 6g–i shows the core level of I 3d XPS spectra in the aged films. As shown in Figure 6d, the Al 2p XPS spectra in the three samples was composed of two Gaussian peaks at 69.5 and 72.2 eV, which matched metal Al and AlI_3, respectively.[58] In addition, we found in the $PC_{61}BM$ ETL-based device that the ratio of AlI_3 to metal Al was much higher than that in the $PC_{61}BM$/ZnO and $PC_{61}BM$/ZnO@PFBC-based devices. It indicated the formation of more AlI_3 due to the chemical reaction between MAI and Al in $PC_{61}BM$ ETL involved cells, which was due to the migration of MAI into the Al top.[37] Meanwhile, the obvious XPS peaks of the I 3 d core levels were also found on the surface of these devices, suggesting the migration of I from the PVSK layer to the film surface. In addition, the intensity of I 3d peaks in the $PC_{61}BM$/ZnO-based devices was higher than that in the $PC_{61}BM$ and $PC_{61}BM$/ZnO@PFBC-based cells. As aforementioned, the ToF–SIMS results have suggested the migration of Zn into the perovskite layer. According to these observations, we can speculate the chemical reaction of PVSK and ZnO. Previous work suggested that the possible reason of the decomposition of PVSK on ZnO was due to an acid–base chemical reaction between the hydroxyl groups on the ZnO surface and MAI ions, as hydroxyl groups and residual acetate were unavoidably left on the ZnO surface for the solution-processable ZnO layer. Such a reaction destroyed the crystal structure of the perovskite, leading to the formation methylamine and PbI_2.[36,44,59] Due to the ZnO accelerated instability issue of the perovskite solar cells, some former works mainly focused on the removal of –OH groups on ZnO NPs through high-temperature annealing,[60] ultraviolet ozone treating,[43] or using other base precursor substitutes.[59] Results demonstrated that decreasing the –OH groups outside the ZnO surface might be a practical approach to improve thermal stability.[59] However, we also found that PFBC modification did not lead to the dramatic decrease of —OH groups on the surface of ZnO from FTIR spectra ("vide infra"). Nevertheless, the ToF–SIMS results suggested the transportation of Zn mass into the perovskite layer for the pristine ZnO. The similar transporting phenomenon of Zn mass was attributed to the asymmetric temperature field by Liu and coworkers.[61] Therefore, we speculated that the removal of –OH groups did not directly contribute to the improvement of thermal stability. However, the removal of surface –OH groups

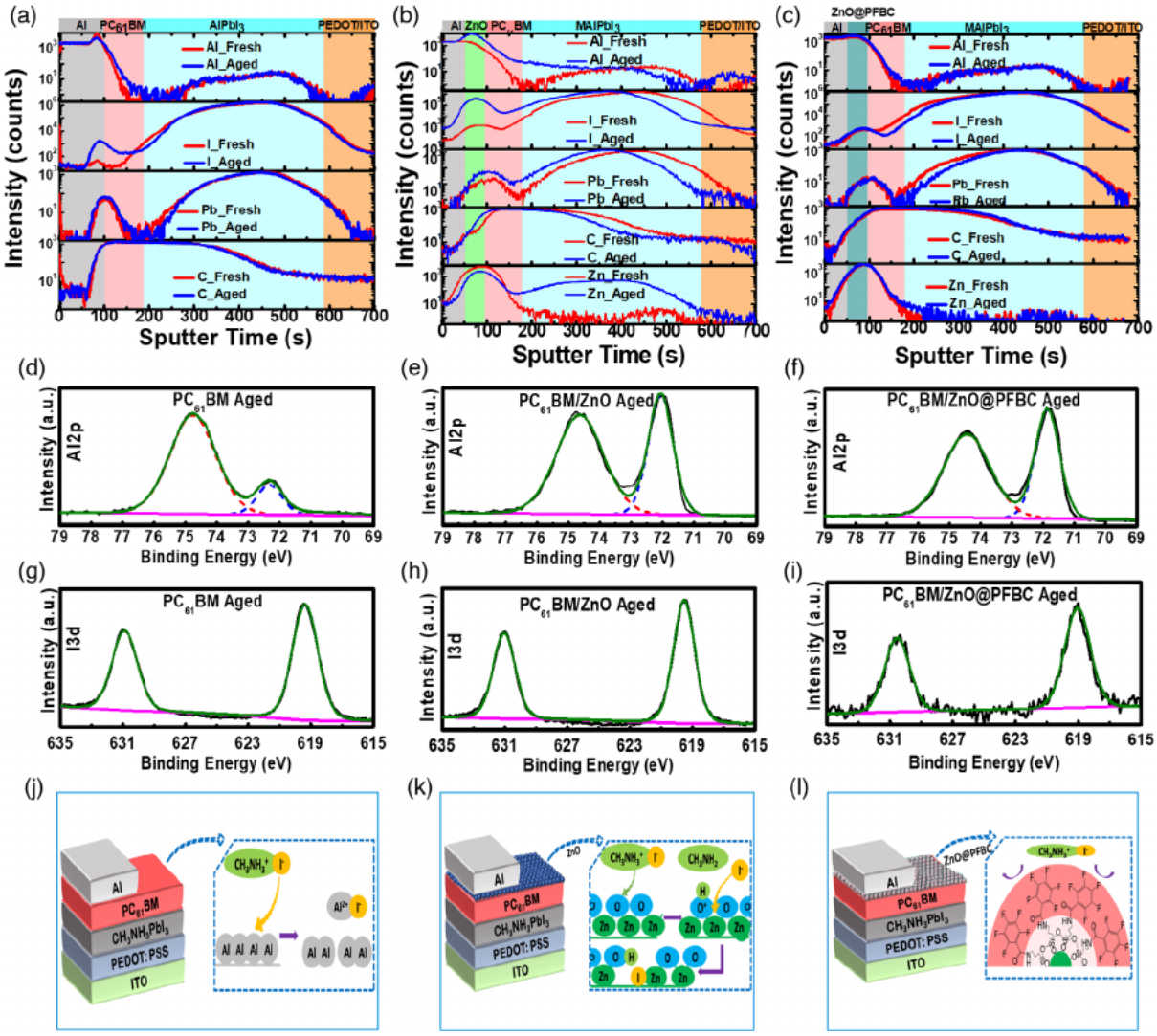

Figure 6. a–c) ToF–SIMS images of the aged devices with $PC_{61}BM$, $PC_{61}BM$/ZnO, and $PC_{61}BM$/ZnO@PFBC ETLs after annealing at 85 °C for 200 h. Core level of XPS spectra of d–f) Al 2p and g–i) I 3d of the fresh and the aged (annealed at 85 °C for 200 h) devices with different ETLs. j–l) Reaction and passivation mechanism.

would lessen the movement of Zn mass and subsequently passivate the reaction of perovskite and ZnO. Herein, in the case of the $PC_{61}BM$/ZnO@PFBC-used device, though the surface OH groups were not removed by PFBC modification, the effective capping of PFBC outside the ZnO NPs would prevent the transportation of Zn mass as well. Consequently, the thermal stability could be significantly proved using PFBC-capped ZnO. Surface XPS spectra showed a negligible Zn 3p peak in the aged ITO/PEDOT: PSS/PVSK/$PC_{61}BM$/ZnO@PFBC films, giving the evidence for the above speculation. In contrast, the $PC_{61}BM$/ZnO films presented a significant increase of the Zn 3p signal, as well as peak shift, which might indicate the formation of ZnI_2.

As previously mentioned, the fast degradation of $PC_{61}BM$ ETL-based solar cell corrosion was due to the migration of I^--induced corrosion of the Al electrode. However the chemical reaction of ZnO and PVSK could accelerate degradation; thus, the pristine ZnO is not suitable for use in the perovskite solar cells. However, the chemical capping of ZnO by PFBC could suppress the ion migration and passivate the chemical reaction of ZnO and perovskite layer, leading to significant improved thermal stability. Based on this explanation, the possible mechanism would be explained, as shown in Figure 6j–l.

Besides thermal stability, long-term stability inside the glove box (Figure 5i) was investigated in this work. The devices were put under 1 sun continuous illumination for more than 45 days, and J–V curves were periodically tested. During continuous illumination, the glove box was cooled by the air conditioner, so the temperature of the devices was kept at around 40 °C. Figure S7, Supporting Information, shows the evolution of V_{OC}, J_{SC}, FF, and PCE during long-term continuous illumination. It is obvious that devices with a sole $PC_{61}BM$ ETL showed a sharp degradation of J_{SC}, which resulted in the quick decrease of PCE within around 200 h. The degradation rate of the

$PC_{61}BM$/ZnO ETL-based solar cell was much slower than the control cells. Specifically, 40% of the initial efficiency remained after 200 h decay. However, the device also nearly died after aging for 1100 h. In comparison with the $PC_{61}BM$ and $PC_{61}BM$/ZnO-involved solar cells, we found an obvious improvement of long-term stability when modifying $PC_{61}BM$ with ZnO@PFBC layer, 60% efficiency remaining after 1100 h long-term continuous illumination. As our previous work has proved that the degradation of the perovskite solar cell under continuous illumination condition in air was ascribed to the unhomogenous coverage of $PC_{61}BM$ layer on the top of the perovskite layer,[10] the improved stability in the glove box for the $PC_{61}BM$/ZnO@PFBC ETL-based cells might be due to the suppression of ion migration as well. For long-term air stability during continuous illumination, these devices were kept at room temperature with humidity about 55%, and the performance decay is shown in Figure S8, Supporting Information. As shown in Figure S8, Supporting Information, all the three devices degraded fast in air. For the pure $PC_{61}BM$ and PCBM/ZnO ETL-based solar cells, device performance could only be maintained for around 30 h. Fortunately, using ZnO@PFBC as a modifier of $PC_{61}BM$ decelerated the degradation process obviously. Because of the hydrophobic properties of the ZnO@PFBC layer, moisture permeation might be lessened in the case of the PCBM/ZnO@PFBC ETL-based solar cell. In all, the improvement of long-term stability during continuous illumination might be also ascribed to the passivation effect of the ion migration of metal electrode and interface chemical reaction by ZnO@PFBC layer.

3. Conclusion

In conclusion, we developed 2,3,4,5,6-pentafluorobenzoyl chloride (PFBC)-capped ZnO NPs through the two-step chemical modifying route. The material can successfully suppress the chemical reaction between the perovskite layer and ZnO, and therefore improve the thermal stability of the perovskite films as directly in contact with ZnO. Consequently, the consistent improvement of long-term stability and air and thermal stability was observed through the addition of this ZnO@PFBC layer on top of the PCBM layer. Further, the deep mechanism was analyzed through TOF–SIMS and XPS spectra. In case of the device with the sole PCBM layer, the corrosion of Al electrode due to halogen ion migration from the perovskite layer to metal electrode was the reason of device degradation. With the addition of ZnO on the top of PCBM, though the corrosion of Al electrode was lessened, the chemical reaction between ZnO and the perovskite layer caused dramatic degradation of the devices. With the ZnO@PFBC modifying PCBM, both the corrosion of the Al electrode and the chemical reaction of ZnO and perovskite were suppressed. This work provides a potential buffer layer based on chemical-tailored ZnO NPs for achieving high performance and good thermal, air, and N_2 storage stability.

4. Experimental Section

Materials: Poly(3,4-ethylenedioxythiophene) polystyrene sulfonate (PEDOT: PSS), methylammonium iodide (MAI), lead iodide (PbI_2), and lead chloride ($PbCl_2$) were obtained from Solarmer Energy, Inc. (Beijing). [6,6]-Phenyl-C_{61}-butyric acid methyl ester ($PC_{61}BM$) was purchased from American Dye Source Inc. ZnO $(OA)_2$. 3-Aminopropyltrimethoxy silane (APTMS) and 2,3,4,5,6-Pentafluorobenzoyl chloride (PFBC) were purchased from J &K Scientific Ltd.

Synthetic Route of ZnO@PFBC NPs: The synthesis of hybrid ZnO NPs was done in different steps that are summarized as follows. The synthesis route for pristine ZnO NPs and APTMS-capped ZnO was followed as reported in the literature.[50] The ZnO@APTMS NPs were washed with toluene several times to remove the unreactive oleic acid-capped NPs. APTMS modification made possible for NPs to be soluble in DMSO, which was used as the reaction medium for dual modification. Pentafluoro benzoyl chloride (PFBC) was added with the same molar concentration of APTMS at 50 °C, and the reaction continued for 4 h. Finally, the colloidal solution of dimethyl sulfoxide (DMSO) resulted in a clear solution. NPs were collected and washed through recrystallization with dichloromethane (DCM). ZnO@pentafluorobenzoylamide (ZnO@PFBC) NPs were dried and stored inside the glove box. For the fabrication process, these hybrid NPs were dissolved in n-butanol to make an ink.

Fabrication of the Perovskite Solar Cells: The hybrid perovskite solar cells were fabricated on top of the patterned indium tin oxide (ITO) glasses with the device architecture of glass/ITO/PEDOT: PSS/PVSK/$PC_{61}BM$/ZnO/Al. ITO patterned glasses were washed with detergent, followed by ultrasonication for 30 min with acetone and isopropanol, and then dried at 80 °C. In the first step, aqueous solution of PEDOT: PSS was spin coated at the speed of 4000 rpm for 40 s. Afterward, the substrate was annealed at 150 °C for 12 min to dry the film and transferred to a N_2-filled glove box for further steps. MAI: $PbI_x/PbCl_{3-x}$ with 1:1 was dissolved in N, N-dimethylformamide (DMF)/DMSO with the concentration of 30 wt%, and the precursor solution was annealed at 70 °C for4 h. The prepared PVSK solution was spin coated with a single-step fabrication method at 6000 rpm for 50 s, and 200 µL toluene was dropped as the antisolvent. Thin-layer perovskite films were heated at 100 °C for 30 min and cooled down at room temperature. $PC_{61}BM$ solution in chlorobenzene with 20 mg mL^{-1} concentration was spin coated on the perovskite thin layer at 1000 rpm for 60 s. The pristine ZnO and ZnO@PFBC NP inks in n-butanol were spin coated as a top protective layer at 1500 rpm for 60 s. The top electrode Al was deposited by thermal evaporation under high vacuum with a 9 or 16 mm^2 effective area for all devices.

Characterization of the ZnO@PFBC NPs and the Solar Cells: The diameter of the ZnO and ZnO@PFBC inks was determined by DLS with Malvern granulometer (Zetasizer Nano). The TEM images of ZnO and ZnO@PFBC were recorded by the EEI Tecani G2 F20 S-Twin 200 kV microscope. FTIR of the ZnO and ZnO@PFBC NPs was recorded by Nicolet 6700 FTIR spectrometer. The absorption spectra were tested by the Lamada 750 UV/Vis/NIR spectrophotometer (PerkinElmer). The PL spectra of the ZnO and ZnO@PFBC NPs were measured in solution with a concentration of 1 mg mL^{-1}. The AFM images of the ZnO and ZnO@PFBC films were recorded by Dimension 3100. UPS and XPS were conducted on a Kratos AXIS Ultra DLD ultrahigh-vacuum (UHV) surface analysis system. The film thickness was characterized using a profiler (VEECO, DEKTAK 150). ToF-SMIS spectra of the fresh and the aged devices were measured by IONTOF TOF-SIMS.5.

The current density–voltage (*J–V*) measurements were carried out in a nitrogen glove box with a Keithley 2400 source meter under a Newport solar simulator (100 mW cm^{-2}). EQE were measured under simulated 1 sun operation conditions with light from a 150 W tungsten halogen lamp (Osram 64610) as the probe light, a monochromator (Zolix, Omni-λ300) for selecting the wavelength, and an *I–V* converter for recording the response. A calibrated Si cell was used as a reference. The test device was kept behind a quartz window in a nitrogen-filled container. The long-term stability in N_2 and in air was conducted through period *J–V* sweeping under continuous illumination in AM 1.5 G. The thermal stability of the devices was conducted through annealing the films on a hot plate for different times and testing the *J–V* characteristics.

Supporting Information

Supporting Information is available from the Wiley Online Library or from the author.

Acknowledgements

The work was financially supported by National Natural Science Foundation of China (51773224), Youth Innovation Promotion Association, CAS (2019317), Natural Science Foundation of Jiangxi Province (20181BAB206017), Natural Science Foundation of Jiangsu Province (BK20181197), Vacuum Interconnected Nanotech Workstation, Suzhou Institute of Nano-Tech and Nano-Bionics, and Chinese Academy of Sciences (CAS).

Conflict of Interest

The authors declare no conflict of interest.

Keywords

ion migrations, perovskite solar cells, thermal stabilities, ZnO electron-transporting layers

Received: June 9, 2020
Revised: July 17, 2020
Published online:

[1] A. Kojima, K. Teshima, Y. Shirai, T. Miyasaka, *J. Am. Chem. Soc.* **2009**, *131*, 6050.
[2] https://www.nrel.gov/pv/cell-efficiency.html (accessed: July 2020).
[3] L. B. Qiu, L. K. Ono, Y. B. Qi, *Mater. Today Energy* **2018**, *7*, 169.
[4] R. Wang, M. Mujahid, Y. Duan, Z. K. Wang, J. J. Xue, Y. Yang, *Adv. Funct. Mater.* **2019**, *29*, 1808843.
[5] Y. G. Rong, Y. Hu, A. Y. Mei, H. R. Tan, M. I. Saidaminov, S. I. Seok, M. D. McGehee, E. H. Sargent, H. W. Han, *Science* **2018**, *361*, 6408.
[6] H. F. Yuan, E. Debroye, K. Janssen, H. Naiki, C. Steuwe, G. Lu, M. Moris, E. Orgiu, H. Uji-i, F. De Schryver, P. Samori, J. Hofkens, M. Roeffaers, *J. Phys. Chem. Lett.* **2016**, *7*, 561.
[7] Y. B. Yuan, J. S. Huang, *Acc. Chem. Res.* **2016**, *49*, 286.
[8] J. P. Correa-Baena, M. Saliba, T. Buonassisi, M. Gratzel, A. Abate, W. Tress, A. Hagfeldt, *Science* **2017**, *358*, 739.
[9] Y. C. Shao, Y. J. Fang, T. Li, Q. Wang, Q. F. Dong, Y. H. Deng, Y. B. Yuan, H. T. Wei, M. Y. Wang, A. Gruverman, J. Shielda, J. S. Huang, *Energy Environ. Sci.* **2016**, *9*, 1752.
[10] S. X. Guo, X. Sun, C. Z. Ding, R. Huang, M. X. Tan, L. P. Zhang, Q. Luo, F. S. Li, J. Jin, C. Q. Ma, *Energy Technol.* **2020**, https://doi.org/10.1002/ente.202000250.
[11] L. Zhou, Z. H. Lin, Z. J. Ning, T. Li, X. Guo, J. Ma, J. Su, C. F. Zhang, J. C. Zhang, S. Z. Liu, J. J. Chang, Y. Hao, *Sol. RRL* **2019**, *3*, 1900096.
[12] J. X. Song, L. J. Liu, X. F. Wang, G. Chen, W. J. Tian, T. Miyasaka, *J. Mater. Chem. A* **2017**, *5*, 13439.
[13] Y. Z. Wu, F. X. Xie, H. Chen, X. D. Yang, H. M. Su, M. L. Cai, Z. M. Zhou, T. Noda, L. Y. Han, *Adv. Mater.* **2017**, *29*, 1701073.
[14] W. H. Zhang, J. Xiong, L. Jiang, J. Y. Wang, T. Mei, X. B. Wang, H. S. Gu, W. A. Daoud, J. H. Li, *ACS Appl. Mater. Interfaces* **2017**, *9*, 38467.
[15] J. K. Zhang, W. J. Mao, J. J. Duan, S. M. Huang, Z. J. Zhang, W. Y. Ou, X. H. Zhang, Z. Sun, X. H. Chen, *Electrochim. Acta* **2019**, *318*, 384.
[16] A. Guerrero, J. B. You, C. Aranda, Y. S. Kang, G. Garcia-Belrnonte, H. P. Zhou, J. Bisquert, Y. Yang, *ACS Nano* **2016**, *10*, 218.
[17] B. J. Zhang, J. Su, X. Guo, L. Zhou, Z. H. Lin, L. P. Feng, J. C. Zhang, J. J. Chang, Y. Hao, *Adv. Sci.* **2020**, *7*, 1903044.
[18] J. W. Li, Q. S. Dong, N. Li, L. Wang, *Adv. Energy Mater.* **2017**, *7*, 1602922.
[19] Y. Kato, L. K. Ono, M. V. Lee, S. Wang, S. R. Raga, Y. Qi, *Adv. Mater Interfaces* **2015**, *2*, 1500195.
[20] H. Lee, C. Lee, *Adv. Funct. Mater.* **2017**, *8*, 1702197.
[21] M. L. Xie, H. Lu, L. P. Zhang, J. Wang, Q. Luo, J. Lin, L. X. Ba, H. Liu, W. Z. Shen, L. Y. Shi, C. Q. Ma, *Sol. RRL* **2018**, *2*, 1700184.
[22] L. F. Zhao, R. A. Kerner, Z. G. Xiao, Y. H. L. Lin, K. M. Lee, J. Schwartz, B. P. Rand, *ACS Energy Lett.* **2016**, *1*, 595.
[23] P. M. Hangoma, Y. C. Ma, I. Shin, Y. L. Liu, W. I. Park, Y. K. Jung, B. R. Lee, J. H. Jeong, S. H. Park, K. H. Kim, *Sol. RRL* **2018**, *3*, 1800289.
[24] D. Yang, X. Zhang, K. Wang, C. Wu, R. Yang, Y. Hou, Y. Jiang, S. Liu, S. Priya, *Nano. Lett.* **2019**, *19*, 3313.
[25] J. Tu, C. Liu, Y. Fan, F. Liu, K. Chang, Z. Xu, Q. Li, Y. Chen, Z. Li, *J. Mater. Chem. A* **2019**, *7*, 15662.
[26] J. H. Heo, S.-C. Lee, S.-K. Jung, O. P. Kwon, S. H. Im, *J. Mater. Chem. A* **2017**, *5*, 20615.
[27] P. Zhang, J. Wu, T. Zhang, Y. F. Wang, D. T. Liu, H. Chen, L. Ji, C. H. Liu, W. Ahmad, Z. D. Chen, S. B. Li, *Adv. Mater.* **2018**, *30*, 1703737.
[28] L.-C. Chen, Z.-L. Tseng, in *Nanostructured Solar Cells*, InTech, London **2017**, p. 204.
[29] Z. L. Zhu, Y. Bai, X. Liu, C. C. Chueh, S. H. Yang, A. K. Y. Jen, *Adv. Mater.* **2016**, *28*, 6478.
[30] S. Bai, Z. W. Wu, X. J. Wu, Y. Z. Jin, N. Zhao, Z. H. Chen, Q. Q. Mei, X. Z. Wang, Z. Ye, T. Y. Song, R. Y. Liu, S. T. Lee, B. Q. Sun, *Nano Res.* **2014**, *7*, 1749.
[31] J. B. You, L. Meng, T. B. Song, T. F. Guo, Y. Yang, W. H. Chang, Z. R. Hong, H. J. Chen, H. P. Zhou, Q. Chen, Y. S. Liu, N. De Marco, Y. Yang, *Nat. Nanotechnol.* **2016**, *11*, 75.
[32] T. Hu, S. Q. Xiao, H. J. Yang, L. Chen, Y. W. Chen, *Chem. Commun.* **2018**, *54*, 471.
[33] S. Z. Zheng, W. L. Li, T. T. Su, F. Y. Xie, J. Chen, Z. Y. Yang, Y. Zhang, S. W. Liu, M. P. Aldred, K. Y. Wong, J. R. Xu, Z. G. Chi, *Sol. RRL* **2018**, *2*, 1700245.
[34] D. Y. Son, J. H. Im, H. S. Kim, N. G. Park, *J. Phys. Chem. C* **2014**, *118*, 16567.
[35] D. Zheng, G. Wang, W. Huang, B. H. Wang, W. J. Ke, J. L. Logsdon, H. Y. Wang, Z. Wang, W. G. Zhu, J. S. Yu, M. R. Wasielewski, M. G. Kanatzidis, T. J. Marks, A. Facchetti, *Adv. Funct. Mater.* **2019**, *29*, 1900265.
[36] K. Schutt, P. K. Nayak, A. J. Ramadan, B. Wenger, Y. H. Lin, H. J. Snaith, *Adv. Funct. Mater.* **2019**, *29*, 1900466.
[37] W. M. Qiu, M. Buffiere, G. Brammertz, U. W. Paetzold, L. Froyen, P. Heremans, D. Cheyns, *Org. Electron.* **2015**, *26*, 30.
[38] X. Y. Zhao, H. P. Shen, Y. Zhang, X. Li, X. C. Zhao, M. Q. Tai, J. F. Li, J. B. Li, X. Li, H. Lin, *ACS Appl. Mater. Interfaces* **2016**, *8*, 7826.
[39] J. L. Yang, B. D. Siempelkamp, E. Mosconi, F. De Angelis, T. L. Kelly, *Chem. Mater.* **2015**, *27*, 4229.
[40] S. S. Mali, J. V. Patil, C. K. Hong, *Adv. Energy Mater.* **2019**, *10*, 1902708.
[41] M. M. Tavakoli, Q. F. Lin, S. F. Leung, G. C. Lui, H. Lu, L. Li, B. Xiang, Z. Y. Fan, *Nanoscale* **2016**, *8*, 4276.
[42] L. J. Zuo, Z. W. Gu, T. Ye, W. F. Fu, G. Wu, H. Y. Li, H. Z. Chen, *J. Am. Chem. Soc.* **2015**, *137*, 2674.
[43] Z. Y. Pang, Y. S. Sun, Y. B. Gao, X. Y. Zhang, Y. F. Sun, J. H. Yang, F. Y. Wang, L. L. Yang, *J. Power Sources* **2019**, *438*, 226957.
[44] M. M. Tavakoli, R. Tavakoli, Z. Nourbakhsh, A. Waleed, U. S. Virk, Z. Y. Fan, *Adv. Mater. Interfaces* **2016**, *3*, 1500790.
[45] F. Yang, D. W. Kang, Y. S. Kim, *RSC Adv.* **2017**, *7*, 19030.
[46] J. Cao, B. H. Wu, R. H. Chen, Y. Y. Q. Wu, Y. Hui, B. W. Mao, N. F. Zheng, *Adv. Mater.* **2018**, *30*, 1705596.

[47] J. Ma, Z. H. Lin, X. Guo, L. Zhou, J. Su, C. F. Zhang, Z. Yang, J. J. Chang, S. Z. Liu, Y. Hao, *Sol. RRL* **2019**, *3*, 1900096.
[48] K. Yao, S. F. Leng, Z. L. Liu, L. F. Fei, Y. J. Chen, S. B. Li, N. G. Zhou, J. Zhang, Y.-X. Xu, L. Zhou, H. T. Huang, A. K. Jen, *Joule* **2019**, *3*, 417.
[49] Z. X. Li, R. Wang, J. J. Xue, X. F. Xing, C. C. Yu, T. Y. Huang, J. M. Chu, K.-L. Wang, C. Dong, Z. T. Wei, Y. P. Zhao, Z. K. Wang, Y. Yang, *J. Am. Chem. Soc.* **2019**, *141*, 17610.
[50] J. F. Wei, G. Q. Ji, C. J. Zhang, L. P. Yan, Q. Luo, C. Wang, Q. Chen, J. L. Yang, L. W. Chen, C. Q. Ma, *ACS Nano* **2018**, *12*, 5518.
[51] D. Costenaro, F. Carniato, G. Gatti, L. Marchese, C. Bisio, *New J. Chem.* **2013**, *37*, 2103.
[52] S. Bai, Y. Z. Jin, X. Y. Liang, Z. Z. Ye, Z. W. Wu, B. Q. Sun, Z. F. Ma, Z. Tang, J. P. Wang, U. Wurfel, F. Gao, F. L. Zhang, *Adv. Energy Mater.* **2015**, *5*, 1401606.
[53] I. Jeon, J. W. Ryan, T. Nakazaki, K. S. Yeo, Y. Negishi, Y. Matsuo, *J. Mater. Chem. A* **2015**, *3*, 20416.
[54] M. Hartel, S. Chen, B. Swerdlow, H. Y. Hsu, J. Manders, K. Schanze, F. So, *ACS Appl. Mater. Interfaces* **2013**, *5*, 7215.
[55] P. N. Murgatroyd, *J. Phys. D-Appl. Phys.* **1970**, *3*, 151.
[56] Y. C. Shao, Z. G. Xiao, C. Bi, Y. B. Yuan, J. S. Huang, *Nat. Commun.* **2014**, *5*, 5784.
[57] J. Seo, S. Park, Y. C. Kim, N. J. Jeon, J. H. Noh, S. C. Yoon, S. I. Sang, *Energy Environ. Sci.* **2014**, *7*, 2642.
[58] J. F. Moulder, W. F. Stickle, P. E. Sobol, K. D. Bomben, *Handbook of X-ray Photoelectron Spectroscopy: A Reference Book of Standard Spectra for Identification and Interpretation of XPS Data*, Physical Electronics Division, Perkin-Elmer Corporation **1992**.
[59] F. Qin, W. Meng, J. C. Fan, C. Ge, B. W. Luo, R. Ge, L. Hu, F. Y. Jiang, T. F. Liu, Y. Y. Jiang, Y. H. Zhou, *ACS Appl. Mater. Interfaces* **2017**, *9*, 26045.
[60] H. X. Liang, Y. C. Hu, Y. R. Tao, B. H. Wu, Y. Y. Wu, J. Cao, *ACS Appl. Mater. Interfaces* **2019**, *11*, 43116.
[61] X. W. Wang, H. Liu, F. Zhou, J. Dahan, X. Wang, Z. P. Li, W. Z. Shen, *ACS Appl. Mater. Interfaces* **2018**, *10*, 835.